# The role of thermal pressurization and dilatancy in controlling the rate of fault slip

**Paul Segall**
Geophysics Department
Stanford University
Stanford, CA, 94305
Email: segall@stanford.edu

**Andrew M. Bradley**
Geophysics Department
Stanford University
Stanford, CA, 94305
Email: ambrad@stanford.edu

*Geophysical observations have shown that transient slow slip events, with average slip speeds v on the order of* $10^{-8}$ *to* $10^{-7}$ *m/s, occur in some subduction zones. These slip events occur on the same faults but at greater depth than large earthquakes (with slip speeds of order* $\sim 1$ *m/s). We explore the hypothesis that whether slip is slow or fast depends on the competition between dilatancy, which decreases fault zone pore pressure p, and thermal pressurization, which increases p. Shear resistance to slip is assumed to follow an effective stress law* $\tau = f(\sigma - p) \equiv f\bar{\sigma}$. *We present two-dimensional quasi-dynamic simulations that include rate-state friction, dilatancy, and heat and pore fluid flow normal to the fault. We find that at lower background effective normal stress (*$\bar{\sigma}$*), slow slip events occur spontaneously, whereas at higher* $\bar{\sigma}$*, slip is inertially limited. At intermediate* $\bar{\sigma}$*, dynamic events are followed by quiescent periods, and then long durations of repeating slow slip events. In these cases, accelerating slow events ultimately nucleate dynamic rupture. Zero-width shear zone approximations are adequate for slow slip events, but substantially overestimate the pore pressure and temperature changes during fast slip when dilatancy is included.*

## 1 Introduction

In the past decade slow slip events (SSE) have been discovered in many subduction zones around the world [1–3], due to anomalous motions in arrays of Global Positioning System (GPS) receivers. Subduction zones, where oceanic plates dive into the mantle, are the sources of the world's largest earthquakes. It is believed that SSE occur on the same faults as, but at greater depths than, mega-thrust earthquakes [1,2]. While the largest subduction zone earthquakes involve slip of tens of meters, last for hundreds of seconds, and have repeat times of centuries, SSE involve slip of centimeters to decimeters, last from weeks to months, and commonly have repeat times of years. Typical slip rates are seven or eight orders of magnitude less than those in regular earthquakes.

There is a great deal of interest in understanding the physical processes that result in slow slip. The study of SSE is also of practical importance: they occur adjacent to the locked megathrust and incrementally increase the shear stress in the zone where damaging quakes nucleate.

*Dilatant strengthening* has been proposed as a mechanism for SSE [4–7]. Dilatancy, the tendency for pore space to increase under shear, is intrinsic to compacted granular materials, including fault gouges. Rate-state frictional weakening allows transient slip to nucleate. As the shear rate increases, pores dilate, and restricted pore fluid flow makes the fault zone increasingly undrained. This decreases pore pressure $p$, increasing the effective normal stress $\bar{\sigma} \equiv (\sigma - p)$, and so increases the frictional resistance to further slip. The faster the fault slips, the harder it is for fluid flow into the fault zone to keep up with dilatancy; thus the stabilizing effect increases with slip speed. However, if slip becomes fast enough, frictional heat is generated faster than can be removed by conduction, leading to *thermal pressurization*. The greater thermal expansivity of water relative to rock leads to an *increase* in $p$ and so a decrease in frictional resistance.

Segall and Rice [8] and Schmitt et al. [9] examined the relative importance of thermal pressurization and rate-state friction during earthquake nucleation in the absence of dilatancy. Schmitt et al. [9] showed that thermal weakening dominates rate and state dependent weakening at slip speeds in excess of roughly $10^{-4}$ to $10^{-2}$ m/s, defined as $v_{\text{crit}}$; the value depending on material properties, including the permeability of the surrounding rocks. In this paper we explore the competition between dilatant strengthening and thermal

pressurization weakening. We previously suggested that dilatant strengthening enables faults with a broad range of thermomechanical parameter values to host SSE [4]. We further hypothesize that SSE occur when dilatancy limits slip speeds to rates less than those for which thermal pressurization dominates fault strength (approximately $v_{\rm crit}$). In contrast, thermal pressurization weakening dominates dilatant strengthening if slip speed exceeds approximately $v_{\rm crit}$, resulting in dynamic (inertially limited) rupture.

This work examines the interactions of rate-state friction on the surfaces of elastic continua, dilatant strengthening, and thermal pressurization, all areas to which Jim Rice has made seminal contributions. We mention only a few key papers here. Rice [10] explained dilatant strengthening on faults with slip-weakening friction. Work with A. Ruina on stability of sliding on surfaces with rate and state dependent friction [11] proved the existence of a critical nucleation dimension for unstable slip, denoted as $h^*$ here and defined in (9). Finally, Rice [12] summarized the key features of thermal pressurization, derived analytical results for weakening with a constant friction coefficient, and showed that the effective fracture energy for this process is consistent with independently derived estimates from seismological observations. This present work in particular owes a considerable debt to Jim's guidance over the years.

## 2 Governing Equations

The fault has uniform thickness $h$ centered on the plane $y=0$. Deformation is assumed to be plane strain in the $x,y$ plane (slip in the x-direction). Inelastic deformation within the fault zone $-h/2 \le y \le h/2$ is approximated by a friction law in which the shear resistance is the product of a friction coefficient and the effective normal stress $\sigma - p(y=0)$ acting on the layer. Pore pressure $p$ is evaluated on the centerline of the shear zone, $y=0$. Fault slip $\delta$ is the integral of the shear strain across the layer. We employ the radiation damping approximation of elastodynamics [13] such that the momentum balance on the fault is

$$\tau_0 + \frac{\mu}{2\pi(1-\nu)} \int_{-\infty}^{\infty} \frac{\partial\delta/\partial\xi}{\xi - x} d\xi - f(v,\theta)[\sigma - p(y=0)] = \frac{\mu}{2v_s} v. \tag{1}$$

The difference between the elastic stress and the frictional resistance is balanced by the stress change associated with plane shear waves (with velocity $v_s$) radiating from the fault. The first term on the left is the shear stress acting on the fault in the absence of slip, the second represents the elastic stress due to gradients in slip $\delta$, and the third term is the frictional resistance. The friction coefficient is a function of sliding velocity $v$ (integral of shear strain rate across the shear zone) and state variable $\theta$. This "quasi-dynamic" formulation leads to a reasonable representation of dynamic slip, although maximum slip speeds and propagation rates are inaccurate [14].

All calculations here are in an elastic full-space. The Hilbert transform in (1) is computed in the Fourier domain. Slip rate, shear stress, and frictional state are computed in the domain $-W/2 \le x \le W/2$, where $W$ is the fault length. The fault is loaded by the constant applied slip rates $v^\infty$ for $W/2 < x < 2W$ and $v = 10^{-4}v^\infty$ for $-2W < x < -W/2$. Assuming initial conditions with zero slip, slip rates vanishingly small relative to $v_s$, and pore pressure in equilibrium with the far-field value $p^\infty$, $\tau_0 = f(v_0,\theta_0)[\sigma - p^\infty]$, where $v_0, \theta_0$ are initial values.

To investigate the role of dilatancy and thermal pressurization during fault slip, we consider coupled friction, dilatancy, heat, and pore fluid flow. Neglecting conduction parallel to the fault (the $x$-direction) and heat advection in the pore fluid phase [15], and assuming spatially uniform thermal properties, the heat equation is [12]

$$\frac{\partial T}{\partial t} = c_{\rm th} \frac{\partial^2 T}{\partial y^2} + \frac{\tau\dot{\gamma}}{\rho c}, \tag{2}$$

where $\dot{\gamma}$ is the shear strain rate, $c$ is specific heat capacity, and $c_{\rm th}$ is thermal diffusivity. For $c_{\rm th} \sim 10^{-6}$ m$^2$/s, a thermal anomaly penetrates on the order of a few meters in the one year cycle time for typical slow slip events. Because this distance is much less than the tens of kilometer dimensions of SSE, gradients in the along-fault direction are likely to be extremely small relative to those in the across-fault direction. Therefore, we can neglect conduction parallel to the fault.

We assume the $y$-dependence of the shear strain-rate can be separated as

$$\dot{\gamma}(x,y,t) = \frac{v(x,t)}{h} g(y), \qquad \text{where} \qquad \int g(y)dy = h. \tag{3}$$

Here $g(y)$ is a specified shaping function that describes how strain rate is distributed across the shearing layer [16]. The thickness of the shear zone can be neglected for times greater than the characteristic conduction time across the layer, typically a few tens of seconds. This is a reasonable assumption for slow slip events lasting days to years, but not for dynamic ruptures with durations of tens to hundreds of seconds. In the limit $h \to 0$, equation (2) reduces to a homogeneous diffusion equation, with the frictional heat production appearing as a boundary condition [12]:

$$\frac{\partial T}{\partial t} = c_{\rm th} \frac{\partial^2 T}{\partial y^2}; \qquad \left.\frac{\partial T}{\partial y}\right|_{y=0} = -\frac{\tau v}{2c\rho c_{\rm th}}. \tag{4}$$

Neglecting pore fluid flow parallel to the fault for the same reason that heat flow in this direction is negligible, changes in pore pressure are given by

$$\frac{\partial p}{\partial t} = \frac{1}{\eta\beta} \frac{\partial}{\partial y}\left(\kappa \frac{\partial p}{\partial y}\right) + \Lambda \frac{\partial T}{\partial t} - \frac{1}{\beta}\frac{\partial \phi}{\partial t}, \tag{5}$$

where $\eta$ is pore fluid viscosity, $\beta$ is the compressibility of the fluid and the pore space, $\kappa$ is the permeability, $\phi$ is

the inelastic component of porosity, and $\Lambda$ is the thermal pressurization parameter, equal to the ratio of thermal expansivity to compressibility [12, 17]. The second term on the right-hand side is thermal pressurization, the third dilatancy/compaction. Dilatancy acts as a fluid pressure sink, whereas thermal pressurization acts as a pressure source. For spatially uniform permeability, the transport term can be written in terms of the hydraulic diffusivity $c_{\rm hyd} = \kappa/\eta\beta$. As for the heat equation, the effect of the shear zone thickness can be neglected for times long compared to the characteristic pore fluid diffusion time across the shear zone. Segall et al. [4] show that, assuming that dilatancy (and compaction) act only normal to the shear zone, $h\dot{\phi} = (1-\phi)\dot{h}$, where $\dot{h}$ is the change in thickness of the shearing layer. In the limit $h \to 0$, and assuming uniform hydraulic properties, the pore pressure diffusion equation reduces to [4]

$$\frac{\partial p}{\partial t} = c_{\rm hyd}\frac{\partial^2 p}{\partial y^2} + \Lambda\frac{\partial T}{\partial t}; \qquad \left.\frac{\partial p}{\partial y}\right|_{y=0} = \frac{h\dot{\phi}}{2\beta c_{\rm hyd}}. \quad (6)$$

### 2.1 Constitutive Laws

Laboratory experiments show that the friction coefficient $f$ depends on the instantaneous slip speed $v$ and the past sliding history, which can be characterized by one or more internal state variables $\theta$. We employ the regularized form of the rate-state equations due to Rice et al. [18], with a single state variable:

$$f(\theta, v) = a\,\text{arcsinh}\left[\frac{v}{2v_0}\exp\left(\frac{f_0 + b\ln(\theta v_0/d_c)}{a}\right)\right]. \quad (7)$$

The material constants $a$ and $b$, which determine the direct velocity and state dependence, respectively, depend on ambient temperature (but are assumed constants here, see [19] for explicit temperature dependence) and hence depth in the earth; $v_0$ is a normalizing constant; and $f_0$ is the nominal friction.

The frictional state is sometimes interpreted as the average asperity contact lifetime, and evolves over a characteristic displacement $d_c$. The proper mathematical description of state evolution has not been resolved (and may not be fully described by any simple analytical representation), although two forms in wide use are the following [20]:

$$\frac{d\theta}{dt} = 1 - \frac{\theta v}{d_c}$$
$$\frac{d\theta}{dt} = -\frac{\theta v}{d_c}\ln\left(\frac{\theta v}{d_c}\right). \quad (8)$$

The first exhibits healing in stationary contact ($v = 0$) and is thus referred to as the "aging" law. In the second form state evolves only with slip ($d\theta/dt$ vanishes when $v = 0$), and is thus referred to as the "slip" law. In both cases the steady-state value of $\theta$ is $d_c/v$. For sufficiently large $v$, the steady-state friction varies with $(a-b)\ln(v/v_0)$.

Rice and Ruina [11] showed that slip on the surfaces of two elastic half-spaces pressed together, with effective normal stress $\bar{\sigma}$ and with steady-state velocity weakening friction ($a - b < 0$), is stable/unstable if the dimensions of the slipping zone are less/greater than a critical nucleation dimension

$$h^* \equiv \frac{d_c\mu/(1-\nu)}{(\sigma - p^\infty)(b-a)}. \quad (9)$$

Here deformation is plane strain, and $\mu$ and $\nu$ are the shear modulus and Poisson's ratio.

Some laboratory studies indicate healing in stationary contact [21,22], and so the aging law is more consistent with available lab data when $\theta$ is far below steady state. However, velocity stepping tests exhibit a symmetric response to step increases and decreases in loading velocity. In addition, the distance scale over which stress decays to steady state following a step velocity increase, when $\theta$ is far above steady state, is nearly independent of the magnitude of the velocity step. Both features are consistent with the slip law but not the aging law [23, 24]. Because nucleation is most sensitive to fault behavior near to and well above steady state [25], the slip law appears to be the more relevant one for nucleation.

Linker and Dieterich [26] interpreted laboratory experiments on frictional response to changes in normal stress as resulting from a change in $\theta$ due to changes in normal stress. These authors suggested that equations (8) be augmented to include the term $-\alpha\theta/b(\sigma-p)d(\sigma-p)/dt$, where $\alpha$ is an additional material constant. If $\alpha > 0$, a fast increase in effective normal stress causes a decrease in $\theta$ and so the friction coefficient; hence the instantaneous change in shear stress is less than would be computed for a constant friction coefficient. All the calculations for this study take $\alpha = 0$. An alternative formulation [27] posits that frictional resistance is the product of a friction coefficient $f(v,\theta)$ and a second state variable that evolves with slip toward the current effective normal stress. In this formulation instantaneous changes in normal stress (at fixed $v$) result in no immediate change in frictional resistance.

We use constitutive laws for the inelastic change in porosity $\delta\phi$, including both dilatancy and compaction, that follow Segall et al. [28] and are motivated in part by experiments of Marone et al. [29]. One form associates dilatancy/compaction with changes in the average lifetime of asperity contacts within the fault gouge [28]:

$$\delta\phi = -\varepsilon\ln\left(\frac{v_0\theta}{d_c}\right) \quad (10)$$

$$\frac{d\phi}{dt} = -\varepsilon\frac{d}{dt}\ln\left(\frac{v_0\theta}{d_c}\right) = -\frac{\varepsilon}{\theta}\frac{d\theta}{dt}, \quad (11)$$

where $d\phi/dt$ is the rate of inelastic change in pore volume and $\varepsilon$ is an empirically derived constant of order $10^{-4}$ [29]. Above steady state, that is, for $\theta > d_c/v$, $\theta$ decreases (from (8)) and the gouge dilates; below steady-state, $\theta$ increases and the gouge compacts.

An alternative form posits a velocity-dependent steady-state porosity, but does not directly associate dilatancy with the frictional state variable [28]. The porosity, however, seeks steady state with the same distance scale as friction, $d_c$, consistent with lab observations:

$$\frac{d\phi}{dt} = -\frac{v}{d_c}(\phi - \phi_{ss}) \tag{12}$$

$$\phi_{ss} = \phi_0 + \varepsilon \ln\left(\frac{v}{v_0}\right). \tag{13}$$

Experiments on fine quartz gouge confirm that the steady-state porosity increases logarithmically with velocity step [30] and lead to estimates of $\varepsilon$ ranging from 0.5 to 3 $\times 10^{-4}$.

For the slip law, the two dilatancy laws are equivalent. Combining (11) with the slip law (8),

$$\begin{aligned}\frac{d\phi}{dt} &= \frac{\varepsilon v}{d_c}\left[\ln\left(\frac{\theta v_0}{d_c}\right) + \ln\left(\frac{v}{v_0}\right)\right] \\ &= -\frac{v}{d_c}\left[\phi - \phi_0 - \varepsilon \ln\left(\frac{v}{v_0}\right)\right],\end{aligned} \tag{14}$$

which is equivalent to the combination of (12) and (13). The second step follows from (10).

The first dilatancy constitutive law (11), which associates dilatancy with state, is inconsistent with an evolution law containing the Linker-Dieterich [26] normal stress term. Consider (11) combined with (8) (here shown with the slip law form, but the same behavior holds for the aging law):

$$\frac{\partial \phi}{\partial t} = -\frac{\varepsilon}{\theta}\frac{d\theta}{dt} = \varepsilon\left[\frac{v}{d_c}\ln\left(\frac{\theta v}{d_c}\right) - \frac{\alpha}{b(\sigma - p)}\frac{dp}{dt}\right]. \tag{15}$$

As $v$ increases, the slip-dependent state evolution causes the porosity to increase. However, an increase in pore pressure cannot sensibly lead to a decrease in porosity. Furthermore, the combination can lead to instability: if increased pore pressure $p$ leads to a decrease in porosity, compaction tends to cause a further *increase* in $p$ (by (5)). As $(\sigma - p)$ decreases, the effect is amplified, leading to instability. At present it is unclear which of the two laws is invalid, but they cannot both be correct. These constitutive equations have been employed by [31], although apparently the choice of parameters did not lead to instability.

To generalize these constitutive equations to distributed shear zones, we first posit that the change in porosity integrated across the shear zone per unit slip $\delta$ (per unit area of fault) does not depend on shear zone thickness $h$:

$$\frac{d}{d\delta}\int_{-h/2}^{h/2}\phi(y,t)\,dy = \int_{-h/2}^{h/2}\frac{\dot{\phi}(y,t)}{v}\,dy \sim 1. \tag{16}$$

The work done on the shear zone by shear traction $\tau$ is $\tau d\delta$; if the fraction of that work that goes into inelastic pore dilation is independent of $h$, then the integrated $d\int \phi dy/d\delta$ must be independent of $h$. Equation (16) implies that $\dot{\phi}(y,t)$ scales with $v/h$.

We seek an expression for $\dot{\phi}(y,t)$ that is consistent with (12) in a thickness-averaged sense. Define thickness-averaged properties by $\langle\cdot\rangle \equiv h^{-1}\int \cdot\, dy$, and let $h_c$ be the shear zone thickness in the experiments from which the coefficient $\varepsilon$ is estimated. The equation

$$\dot{\phi}(y,t) = -\frac{v h_c}{d_c h}[\phi(y,t) - \phi_{ss}(y,t)] \tag{17}$$

has the appropriate scaling (16) and reduces to (12) when $h = h_c$ and $\phi$ and $\phi_{ss}$ are thickness averaged.

We further require the thickness-averaged $\phi_{ss}$ to be independent of $h$, which implies

$$\int_{-h/2}^{h/2}\phi_{ss}(y,t)\,dy \sim h. \tag{18}$$

The net porosity change, proportional to the change in shear zone thickness, scales linearly with $h$. This is supported by experimental data of [32] (C. Marone, person. comm.).

Since we do not consider strain localization (or delocalization) here, it is reasonable to assume that the space and time dependence of $\phi_{ss}$ are separable. For example, writing $\phi_{ss}(y,t) = \hat{\phi}_{ss}(t)g(y)$, where recall that $\int_{-h/2}^{h/2} g(y)\,dy = h$, satisfies (18) and makes the change in porosity proportional to the shear strain. The obvious extension of (13) is thus

$$\langle\phi_{ss}\rangle = \hat{\phi}_{ss}(t) = \phi_0 + \varepsilon \log\frac{v}{v_0}. \tag{19}$$

If the intial condition $\phi(y,0)$ is also proportional to $g(y)$, then $\phi(y,t) = \hat{\phi}(t)g(y)$ for all time. Thus, from (17)

$$\frac{d\phi(y,t)}{dt} = -\frac{v h_c}{d_c h}g(y)[\hat{\phi}(t) - \hat{\phi}_{ss}(t)] \tag{20}$$

$$= -\frac{h_c}{d_c}\dot{\gamma}(y)[\hat{\phi}(t) - \hat{\phi}_{ss}(t)]. \tag{21}$$

Introducing the steady-state response (19),

$$\frac{d\phi(y,t)}{dt} = -\frac{v(t)h_c}{hd_c}g(y)\left[\hat{\phi}(t) - \phi_0 - \varepsilon\ln\left(\frac{v(t)}{v_0}\right)\right] \tag{22}$$

$$\frac{d\hat{\phi}(t)}{dt} = -\frac{v(t)h_c}{hd_c}\left[\hat{\phi}(t) - \phi_0 - \varepsilon\ln\left(\frac{v(t)}{v_0}\right)\right]. \tag{23}$$

In summary, this formulation predicts that the dilatancy approach to steady state scales with $hd_c/h_c$. For example, a doubling of the shear zone thickness will double the effective $d_c$ for dilatancy and leave the value of $\varepsilon$ the same.

Similarly, it is also reasonable that the critical slip distance for friction should scale with layer thickness, consistent with laboratory data of [32]. $d_c$ for nominally bare surfaces is thought to be related to average asperity dimensions.

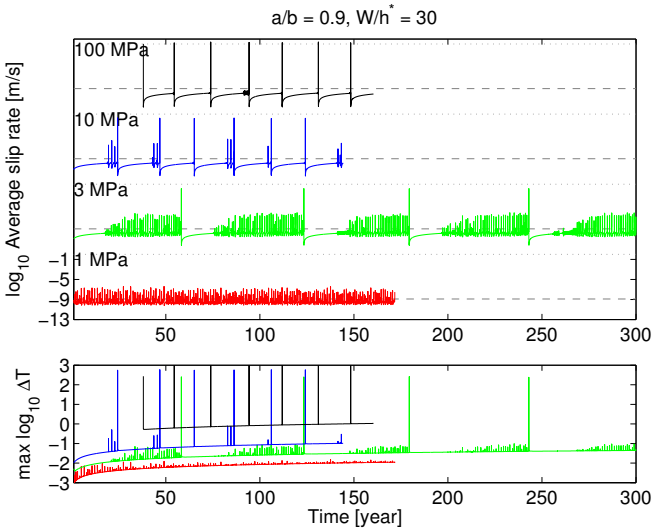


Fig. 1. a) Spatially averaged slip speed as a function of time for four different values of background effective stress: 1, 3, 10, and 100 MPa. Dashed line indicates $v^\infty$. In all cases $a/b = 0.9$ and $W/h^* = 30$. b) Maximum $\Delta T$ (°C) on the fault as a function of time.

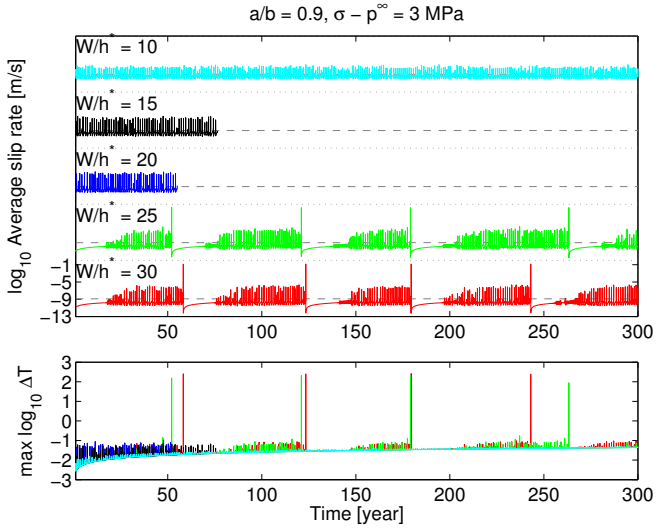


Fig. 2. a) Spatially averaged slip speed as a function of time for four different values of $W/h^*$ at fixed $\bar{\sigma} = 3$ MPa and $a/b = 0.9$. Dashed line indicates $v^\infty$. b) Maximum $\Delta T$ (°C) on the fault.

In particulate gouges, slip occurs between grains; therefore, if the shear is distributed across a thicker zone, slip at the grain scale is on average diminished. Thus, it takes more macroscopic slip to bring a new set of asperities into contact at the grain scale. Since laboratory data [29, 30] show that the effective $d_c$ for dilatancy and friction are comparable, we assume that both scale linearly with $h$, as in (23). Thus, changing the thickness of the shearing layer has three effects: it changes the slip required to achieve steady state for both dilatancy and friction, and it also changes the source term in the heat equation (equations (2) and (3)).

### 2.2 Dimensional Analysis

To clarify the role of thermal pressurization relative to dilatant strengthening, we explore a non-dimensionalization of the governing equations. Take non-dimensional time, pore pressure, stress, and temperature to be $\tilde{t} = tv^\infty/d_c$, $\tilde{p} = p/(\sigma - p^\infty)$, $\tilde{\tau} = \tau/f_0(\sigma - p^\infty)$, $\tilde{T} = \Lambda T/(\sigma - p^\infty)$. State is non-dimensionalized in the same way as time, and $\tilde{v} = v/v^\infty$. As in [4], this leads to non-dimensional parameters related to friction and elasticity: $a/b < 1$, $f_0/b \simeq 30$, and $W/h^*$, and non-dimensional radiation damping parameter $\mu v^\infty/2b(\sigma - p^\infty)v_s \ll 1$ .

In the finite-width case, we take $\tilde{y} = y/h$, whereas in the zero-width case there is no natural length scale and so we take $\tilde{y} = \sqrt{y^2 v^\infty/c_{\rm hyd} d_c}$. With this scaling and dilatancy law (11), Segall et al [4] found three additional non-dimensional parameters: $c_{\rm th}/c_{\rm hyd}$, $E_T$, and $E_p$, where the thermal and dilatancy "efficiencies" arise through the boundary conditions and

$$E_T = \frac{f_0\Lambda}{2\rho c_p}\sqrt{\frac{c_{\rm hyd} d_c v^\infty}{c_{\rm th}^2}}, \qquad E_p = \frac{\varepsilon}{2\beta(\sigma - p^\infty)}\sqrt{\frac{h^2 v^\infty}{c_{\rm hyd} d_c}}. \tag{24}$$

In the finite-width case, and normalizing $\hat{\phi}$ and $\hat{\phi}_{\rm ss}$ by $\varepsilon$, the transport equations yield the following non-dimensional parameters: $c_{\rm th}/c_{\rm hyd}$, $d_c/h$, $c_{\rm hyd} d_c/v^\infty h^2$, $f_0\Lambda/\rho c$, and $\varepsilon h_c/h\beta(\sigma - p^\infty)$. Of particular interest for understanding the tendency for slow versus fast slip is the ratio of the dilatancy to shear heating source terms. In the finite-width case this ratio is

$$\frac{\varepsilon\rho c_p}{f_0\Lambda\beta(\sigma - p^\infty)}\left(\frac{h_c}{d_c}\right). \tag{25}$$

Dilatant strengthening is favored at low nominal effective stresses $\bar{\sigma}$, consistent with seismological observations in some areas where SSE occur [4] . In contrast, high $\bar{\sigma}$ favors thermal pressurization and fast slip.

## 3 Results: Zero Thickness and Uniform Properties

We begin by exploring solutions with spatially uniform properties in the limit of negligible shear zone thickness. For the sake of simplicity we fix the following parameters: $a/b = 0.9$, $f_0/b = 33.33$, $c_{\rm th}/c_{\rm hyd} = 1.0$, and $E_T = 3.0 \times 10^{-5}$. In the first set of numerical experiments we systematically vary the background effective stress $\sigma - p^\infty$ for fixed $W/h^*$. Note that $E_p$, $h^*$, and the non-dimensional radiation damping parameter are all functions of effective stress; in particular, for fixed ratio $W/h^*$, low effective stress corresponds to large fault length $W$.

Summary results are shown in Figure 1 for $W/h^* = 30$. All computations are for grid dimension along the fault that satisfy $\Delta x \le L_d/15$, where $L_d \equiv (1 - a/b)h^*$ [25]. For $a/b = 0.9$ this means $\Delta x \le h^*/150$. For $\sigma - p^\infty \ge 3$ MPa the fault exhibits inertially limited slip with spatially averaged (over domain $-W/2 \le x \le W/2$) slip speeds of 0.1 m/s or more (maximum slip speeds are considerably higher), while for $\sigma - p^\infty = 1$ MPa the system exhibits only stable transient slip events with average slip rates somewhat in excess of $10^{-8}$

m/s. The behavior at 3 MPa shows fast slip, followed by a decade of stable sliding, before transient events develop. These can last for decades before the next dynamic event occurs. At 10 MPa, there are only a few stable transients prior to dynamic instability, and at 100 MPa the system for the most part exhibits only dynamic events.

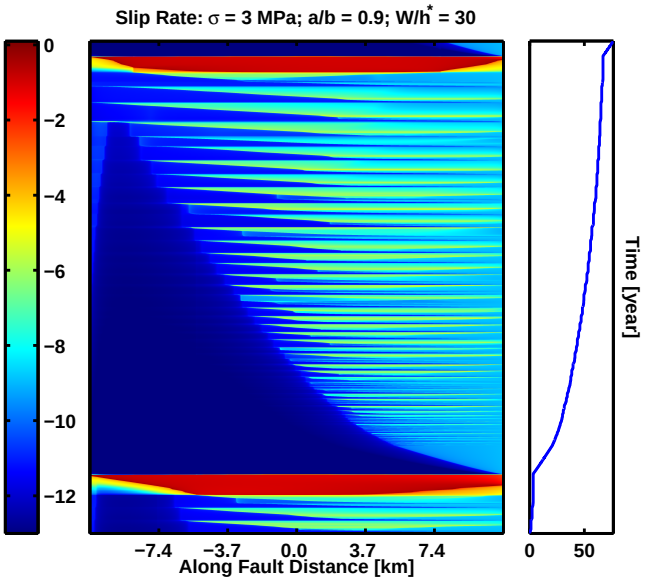


Fig. 3. Space-time evolution of slip-rate for $\sigma_{\rm eff} = 3$ MPa, and $W/h^* = 30$. The color scale is $\log_{10}(v)$. The vertical axis of the main and right plots is solver step; in the right box, time (yr) is plotted as a function of solver step. The solver takes small time steps during fast slip and larger time steps when slip is stable.

Also shown in Figure 1 is the maximum temperature excursion. Between dynamic events the temperature change is small ($< 1°$C) with very modest increases during model slow slip events. Not surprisingly, dynamic events are associated with strong temperature spikes of order hundreds of degrees. At 100 MPa the temperature spikes exceed 1000°C (and might be larger in a fully dynamic solution since radiation-damping underestimates $v$); we discuss this in more detail below. At 1 MPa the temperature changes are sufficiently small that isothermal calculations [4] are appropriate. The gradual increase in $T$ is due to the system coming to long-term thermal steady state.

We next examine the behavior for fixed effective stress of 3 MPa and variable $W/h^*$ (Fig. 2). As expected, sufficiently short slip zones (e.g., $W/h^* \leq 20$) exhibit repeating SSE, whereas for $W/h^* = 30$ there are dynamic events as in Figure 1.

The space-time evolution of slip rate for the 3 MPa case is examined in Figure 3. Following a dynamic event that ruptures the entire fault, there is a long period of stable sliding (see also Figure 1) in which the slipping area propagates into the effectively locked region. After roughly ten years slow slip events initiate; with increasing time these events propagate further into the effectively locked region. As the length of the slipping zone increases, the maximum slip rate also increases, becoming of the order of $10^{-5}$ m/s. Eventually, one of the slow slip events nucleates a dynamic event.

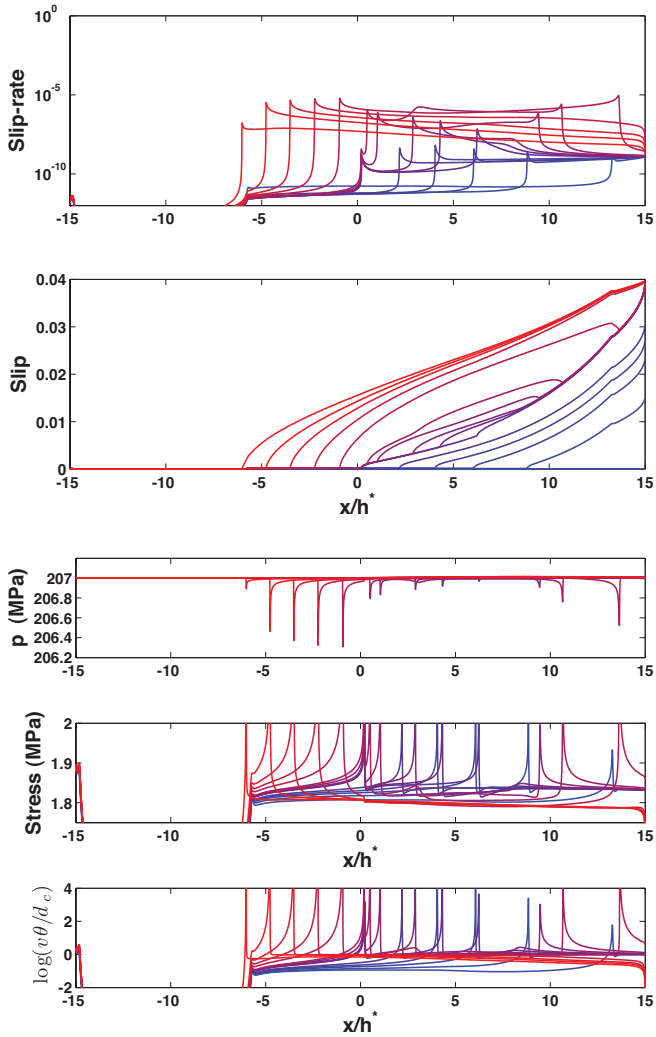


Fig. 4. a) Slip rate (m/s), b) slip (m), c) fault zone pore pressure (MPa), d) shear stress (MPa), and e) $\log(v\theta/d_c)$ as a function of along-fault distance during a slow-slip cycle. $\sigma_{\rm eff} = 3$ MPa, $W/h^* = 30$. Curves represent snapshots in time, not equally spaced, grading from blue to red.

The behavior during a slow slip cycle is shown in Figure 4. As has been observed in isothermal calculations [4], slow slip events are preceded by up-dip propagation of slip driven by the constant velocity boundary condition (Figure 4b). In the example here this phase lasts for approximately one year. Slip is stabilized by slight (order 0.1 MPa) reductions in pore pressure near the rupture tips caused by dilatancy (Figure 4c). This phase is associated with stress accumulation (Figure 4d) rather than release, and slip brings the fault close to steady-state frictional conditions (Figure 4e). At some point slip begins to accelerate near $x/h^* \sim 7$, propagating first up-dip and then bilaterally. Max-

imum slip speeds reach approximately $10^{-5}$ m/s; this faster phase lasts for slightly more than a day in this simulation. The faster phase is also stabilized by dilatancy-induced decreases in pore pressure of order 0.6 MPa near the rupture tips, and is accompanied by modest stress drops of order 0.05 MPa (Figure 4d). The model slow slip events are associated with slight increases in fault temperature; however, these do not exceed 0.1°C (Fig. 1).

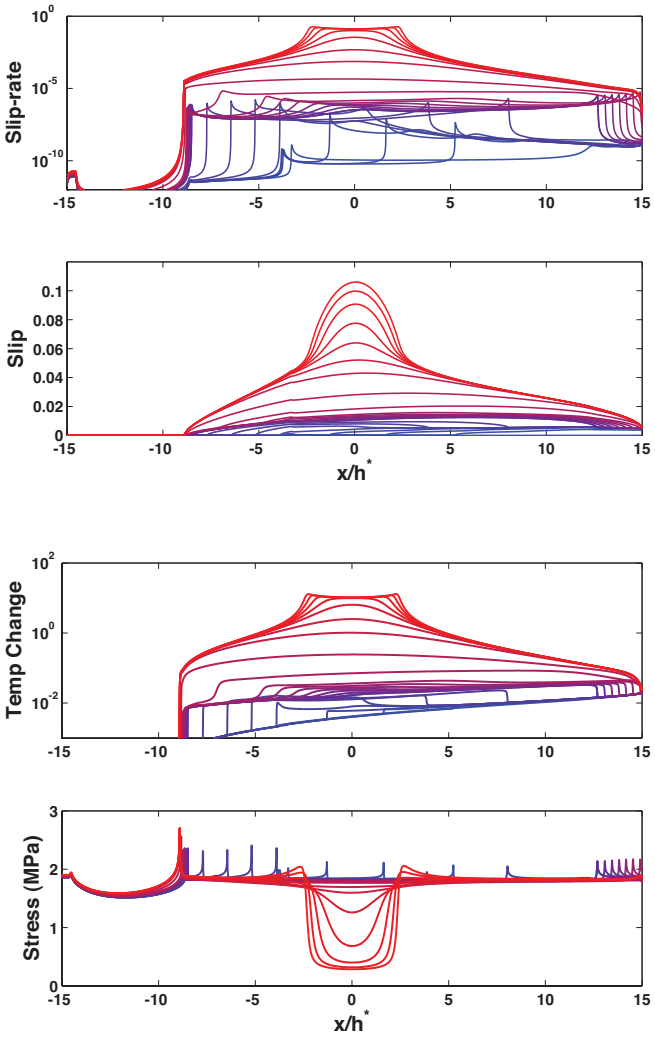


Fig. 5. a) Slip rate (m/s), b) slip (m), c) temperature change (°C), and d) shear stress (MPa) as a function of along-fault distance. $\sigma_{\text{eff}} = 3$ MPa, $W/h^* = 30$. Curves represent snapshots in time, not equally spaced, grading from blue to red.

As can be seen from Figure 3, slow slip events continue for some time, penetrating increasingly farther into the effectively locked zone. The transition from slow slip to a dynamic event is shown in Figures 5, which starts with a slow slip event that propagates from right to left, followed by bilateral propagation at rates well below $10^{-5}$ m/s. Propagation during this period is stabilized by dilatancy-induced pore pressure reduction and consequent increase in shear resistance (Figure 5d). Further acceleration in the central region, near $x = 0$, causes an increase in temperature (Figure 5c), the onset of thermal pressurization, and a marked stress drop (Figure 5d). At this point the slip speeds have reached radiation damping limits and the rupture propagates bilaterally. The shear strength begins dropping dramatically at slip speeds of approximately $10^{-5}$ m/s, which we can consider a critical slip speed for thermal pressurization to dominate the fault strength, as in [9].

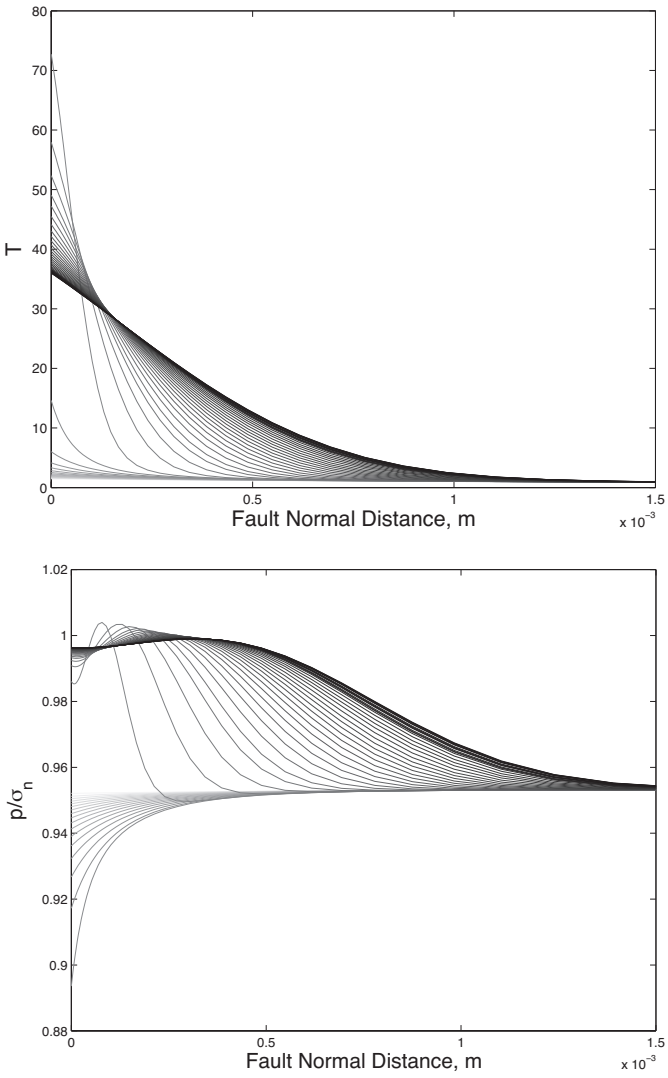


Fig. 6. Temperature, °C (top) and pore pressure (bottom) as a function of distance normal to the fault; zero-width fault approximation. Background effective stress is 10 MPa. Curves represent different snapshots in time, not regularly spaced, from light to dark. Dilatancy initially leads to a decrease in pore pressure, followed by thermally induced pressurization.

Figure 6 shows profiles of temperature and pore pressure as a function of distance perpendicular to the fault as a rupture front propagates past. This calculation is for a

background effective stress of 10 MPa and the zero-width approximation. Initially, dilatancy causes a reduction in pore pressure and a consequent increase in effective stress. After some amount of slip, frictional heating causes the temperature to increase, and thermal pressurization overwhelms dilatancy, causing an increase in pore pressure. The boundary condition on pore pressure (equation 6) states that for positive $d\phi/dt$ the gradient is positive, and so pore pressure is a local minimum on the fault. This can lead to a significant local maximum in pore pressure off the fault. There is indeed nothing in the mathematical formulation that prevents the pore pressure from exceeding the fault-normal compressive stress, as is seen in Figure 6.

For a nominal effective stress of 100 MPa, the temperature rise and the off-fault pore pressure maximum become even more acute. As the rupture front passes, dilatancy initially causes an extreme reduction in pore pressure, even becoming negative. The large pressure decline causes the effective stress to rise substantially, leading to extreme transient heating; in this case the temperature transiently exceeds 1500°C. The extreme temperature rise off the fault leads to off-fault pore pressures that exceed the fault normal stress by a factor of almost two. The extreme behavior occurs within 100 microns of the fault, which is comparable to the thickness of principal shear zones on faults [12]. The characteristic diffusion time across the shear zone is negligible compared to the duration of slip for SSE; however, this is not the case for dynamic events. Thus, one must account for the finite width of the shear zone during dynamic events [33], as discussed in the following section.

Otherwise identical calculations ($\sigma_{\rm eff} = 3$ MPa) without dilatancy ($\varepsilon = 0$) lead to temperatures that never exceed 250°C and pore pressures that approach the fault-normal stress but decrease monotonically away from the fault. Rice [12] provides an analytical result for the maximum temperature change for constant coefficient of friction and no dilatancy: $T_{max} - T_{amb} = (1 + \sqrt{c_{\rm hyd}/c_{\rm th}})(\sigma - p_0)/\Lambda$. In these calculations $c_{\rm hyd} = c_{\rm th}$ and $\Lambda = 0.8$ MPa/°C, leading to $T_{max} - T_{amb} = 250$°C, as observed numerically.

Dilatant pore volume expansion is expected to evolve on slip scales short compared to the evolution of $T$ and $p$. In this case and in the undrained and adiabatic limits for a finite-thickness shear zone the effect of dilatancy is to decrease the initial pressure by $-\delta\phi/\beta$ [12]. More generally, $-\delta\phi/\beta$ is an upper bound on the pore pressure drop. This is not the case, however, for a zero-width shear zone, for which the diffusive fields can become unbounded for sufficiently fast processes. In Appendix B we examine the solution to the coupled temperature and pore pressure equations for constant slip speed $v$ and coefficient of friction, including the effect of dilatancy. We find that the dilatancy induced pore fluid suctions can significantly exceed $-\delta\phi/\beta$. Furthermore, the influence of these pore suctions on the fault temperature is not simply found by modifying the initial pressure to account for the dilatant suction. In short, the limitations of the $h \to 0$ model are more severe when including the effects of dilatancy.

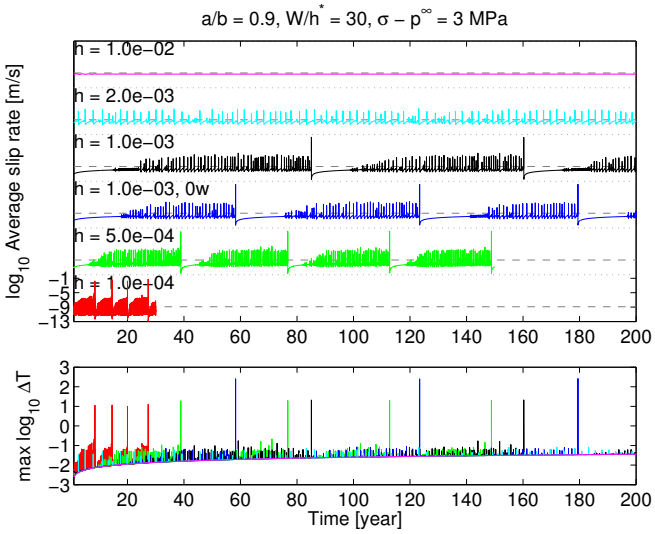


Fig. 7. Results for finite-width shear zone; $a/b = 0.9$, $W/h^* = 30$, and $\sigma - p^\infty = 3$ MPa. a) Spatially averaged slip speed as a function of time for different shear zone thicknesses $h$ (in meters). $h_c = 10^{-3}$. The case $h = 10^{-3}$,0w refers to the zero-width approximation. b) Maximum $\Delta T$ (°C) on the fault as a function of time.

## 4 Results: Finite Thickness and Uniform Properties

In this section we consider calculations with finite-thickness shear zones. Figure 7 shows average slip speed and maximum temperature rise for a range of shear zone thicknesses. The first thing to notice is that the the system behavior for the $h = 1$mm case and the zero-width approximation of the same thickness is very similar, except that the maximum temperature change during dynamic slip events is much reduced, as expected. Recall that $h$ appears in the boundary condition (6) in the zero-width approximation.

In these calculations the characteristic slip distance for both friction and dilatancy scale with shear layer thickness. As the layer thickness increases, the effective $d_c$ increases, and the shear is spread over a greater volume of fault gouge, reducing the temperature rise; both effects are stabilizing and slip becomes completely steady when $h$ is increased to 10 mm. On the other hand, reducing $h$ makes the system less stable. However, even for $h$ of 100 $\mu$m the system still responds with transient slow slip events. In this case dynamic events occur much more frequently, although the maximum temperature increases are only on the order of 10°C.

We compare the temperature and pore pressure distributions normal to the fault in the finite-width case in Figure 8 for a background effective stress of $\sigma - p^\infty = 100$ MPa, $h = 100\mu$m, and $d_c = 10\mu$m. In this simulation the effective $d_c$ for dilatancy (only) was scaled by $h/h_c = 1/10$. Thus, the effective $d_c$ for dilatancy is extremely small and the consequent increase in effective stress occurs with very little slip. Even so, the temperature rise is limited to 200°C, compared to $> 1000$°C in the zero-width case. The pore pressure reaches roughly $0.95\sigma$ but is everywhere less than the fault normal stress. For the identical case without dilatancy the maximum temperature rise was reduced, but only by about 5

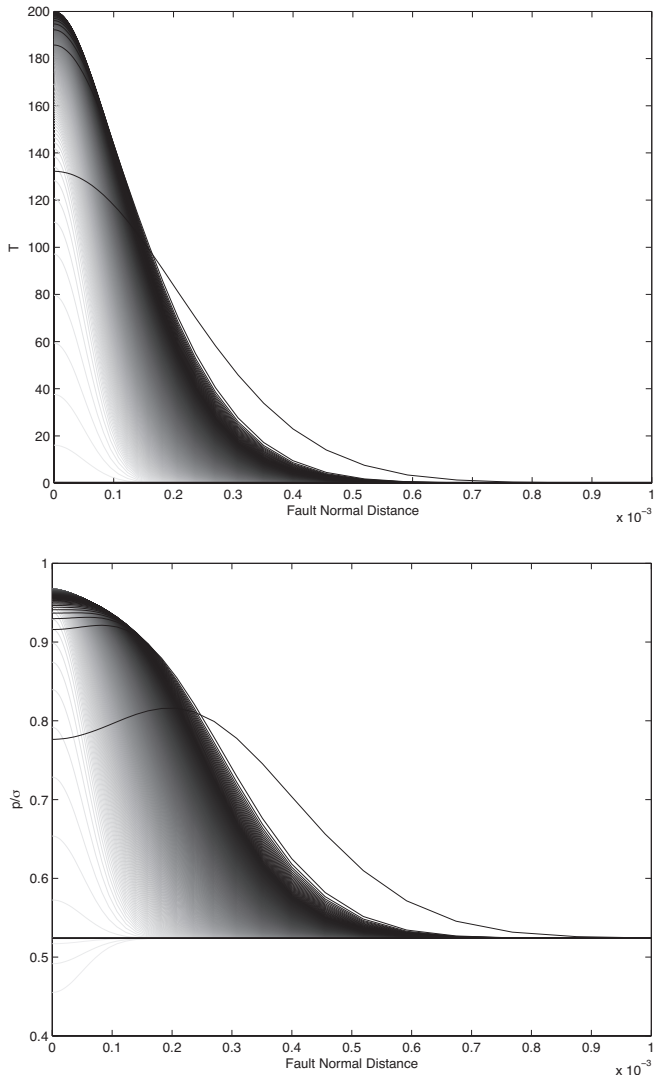


Fig. 8. a) Temperature (°C) and b) pore pressure profiles as a function of distance normal to the fault during a dynamic slip event. In this calculation $h = 100\mu$m, $d_c = 10\mu$m. In this simulation the effective $d_c$ for dilatancy was scaled by $h/h_c = 1/10$. $\sigma - p^\infty = 100$ MPa, $W/h^* = 30$.

to 10%.


## Achnowledgements

We gratefully acknowledge support from the National Science Foundation (EAR-0838267), the U.S. Geological Survey (08HQGR0014), and the Southern California Earthquake Center. We thank Chris Marone for discussions on dilatancy, and both reviewers for comments which improved the readability of the paper.


## References


[1] Schwartz, S., and Rokosky, J., 2007. "Slow slip events and seismic tremor at circum-pacific subduction zones". *Reviews of Geophysics,* **45**, p. RG3004.

[2] Peng, Z., and Gomberg, J., 2010. "An integrated perspective of the continuum between earthquakes and slow-slip phenomena". *Nature GeoScience,* **3**, pp. 399 – 607, doi:10.1038/ngeo940.

[3] Beroza, G. C., and Ide, S., 2011. "Slow earthquakes and nonvolcanic tremor". *Annu. Rev. Earth Planet. Sci.,* **39**, pp. 271 –296.

[4] Segall, P., Rubin, A., Bradley, A. M., and Rice, J., 2010. "Dilatant strengthening as a mechanism for slow slip events". *Jour. Geophys. Res.,* **115**, p. 37.

[5] Suzuki, T., and Yamashita, T., 2009. "Dynamic modeling of slow earthquakes based on thermoporoelastic effects and inelastic generation of pores". *Journal of Geophysical Research,* **114**, p. B00A04.

[6] Liu, Y. J., and Rubin, A., 2010. "Role of fault gouge dilatancy on aseismic deformation transients". *Journal of Geophysical Research,* **115**, p. B10414.

[7] Yamashita, T., and Suzuki, T., 2011. "Dynamic modeling of slow slip coupled with tremor". *Jour. Geophys. Res.,* **116 B05301**, p. doi:10.1029/2010JB008136.

[8] Segall, P., and Rice, J. R., 2006. "Does shear heating of pore fluid contribute to earthquake nucleation?". *J. Geophys. Res.,* **111**, p. B09316.

[9] Schmitt, S. V., Segall, P., and Matsuzawa, T., 2011. "Shear heating induced thermal pressurization during earthquake nucleation". *Jour,* **116**, p. doi:10.1029/2010JB008035.

[10] Rice, J., 1975. "Stability of dilatant hardening for saturated rock masses". *Journal of Geophysical Research,* **80**(11), pp. 1531–1536.

[11] Rice, J., and Ruina, A., 1983. "Staibility of steady frictional slipping". *Journal of Applied Mechanics-Transactions of the ASSME,* **50**(2), pp. 343–349.

[12] Rice, J. R., 2006. "Heating and weakening of faults during earthquake slip". *J. Geophys. Res.,* **111**, p. B05311.

[13] Rice, J., 1993. "Spatio-temporal complexity of slip on a fault". *Journal of Geophysical Research,* **98**, pp. 9885–9907.

[14] Lapusta, N., and Liu, Y., 2009. "Three-dimensional boundary integral modeling of spontaneous earthquake sequences and aseismic slip". *Journal of Geophysical Research,* **114**, p. B09303.

[15] Lachenbruch, A. H., 1980. "Frictional heating, fluid pressure, and the resistance to fault motion". *Journal of Geophysical Research,* **85**, pp. 6097–6112.

[16] Andrews, D. J., 2002. "A fault constitutive relation accounting for thermal pressurization of pore fluid". *J. Geophys. Res.,* **107**(B12).

[17] Bizzarri, A., and Cocco, M., 2006. "A thermal pressurization model for the spontaneous dynamic rupture propagation on a three-dimensional fault: 1. Methodological approach". *J. Geophys. Res.,* **111**, p. B05303.

[18] Rice, J. R., Lapusta, N., and Ranjith, K., 2001. "Rate and state dependent friction and the stability of sliding between elastically deformable solids". *Journal of Mechanical and Physical Solids,* **49**, pp. 1865–1898.

[19] Bizzarri, A., 2011. "Temperature variations of consti-

tutive parameters can significantly affect the fault dynamics". *Earth and Planetary Science Letters .,* **306, doi:10.1016/j.epsl.2011.04.009**, pp. 272–278.

[20] Marone, C., 1998. "Laboratory-derived friction laws and their application to seismic faulting". *Ann. Rev. Earth Planet. Sci,* **26**, pp. 643–696.

[21] Dieterich, J. H., and Kilgore, B. D., 1994. "Direct observation of frictional contacts: new insights for state-dependent properties". *Pure. Appl. Geophs.,* **143**, pp. 283–302.

[22] Beeler, N., Tullis, T. E., and Weeks, J., 1994. "The roles of time and displacement in the evolution effect in rock friction". *Geophys. Res. Lett.,* **21**, pp. 1987 – 1990.

[23] Ruina, A., 1983. "Slip instability and state variable friction laws". *J. Geophys. Res.,* **88**(B12), pp. 10359–10370.

[24] Bayart, E., Rubin, A. M., and Marone, C., 2006. "Evolution of fault friction following large velocity jumps,". In Eos Trans. AGU,87(52), Fall Meet. Suppl., Abstract S31A-0180.

[25] Ampuero, J.-P., and Rubin, A. M., 2008. "Earthquake nucleation on rate and state faults—aging and slip laws". *J. Geophys. Res.,* **113**, p. B01302.

[26] Linker, M. F., and Dieterich, J. H., 1992. "Effects of variable normal stress on rock friction: Observations and constitutive equations". *J. Geophys. Res.,* **97**(B4), pp. 4923–4940.

[27] Prakash, V., 1998. "Frictional response of sliding interfaces subjected to time varying normal pressures". *Journal of Tribology,* **120**, pp. 97–102.

[28] Segall, P., and Rice, J. R., 1995. "Dilatancy, compaction, and slip instability of a fluid-infiltrated fault". *J. Geophys. Res.,* **100**(B11), pp. 22155–22171.

[29] Marone, C., Raleigh, C., and Scholz, C., 1990. "Frictional behavior and constitutive modeling of simulated fault gouge". *Journal of Geophysical Research,* **95**, pp. 7007–7025.

[30] Samuelson, J., Elsworth, D., and Marone, C., 2009. "Shear-induced dilatancy of fluid-saturated faults: Experiment and theory". *Journal of Geophysical Research,* **114**, p. B12404.

[31] Mitsui, Y., and Cocco, M., 2010. "The role of porosity evolution in frictional instabilities: A parametric study using a spring-slider dynamic system". *Geophysical Research Letters,* **37, L23305**, p. doi:10.1029/2010GL045672.

[32] Marone, C., and Kilgore, B., 1993. "Scaling of the critical slip distance for seismic faulting with shear strain in fault zones". *Nature,* **362**, pp. 618–621.

[33] Noda, H., Dunham, E. M., and Rice, J. R., 2009. "Earthquake ruptures with thermal weakening and the operation of major faults at low overall stress levels". *J. Geophys. Res.,* **114**, p. B07302.

[34] Bogacki, P., and Shampine, L., 1989. "A 3(2) pair of Runge-Kutta formulas". *Appl. Math. Lett.,* **2**(4).

## Appendix A: Numerical Solution

We describe the numerical methods employed in the software Fault Dynamics with a Radiation-damping Approximation (FDRA). FDRA solves the equations of momentum balance (1), heat (2 or 4) and pore fluid pressure (5 or 6) diffusion, state evolution (8), and porosity evolution (23).

**The diffusion equations.** Let us write a diffusion equation for a general diffusive quantity $q$; those for pressure $p$ and temperature $T$ follow this form.

The diffusion equations are discretized in space using finite differences on a nonuniform mesh. To capture steep gradients in $p$ and $T$ that occur in and near the shear zone, we use the following change of coordinate between $y$ and $z$: $z(y) = \log(c+y)$, with $c = 10^{-6}$.

Let the original PDE be

$$\begin{aligned} \dot{q} &= (aq_y)_y + f \\ q_y(0,t) &= g_0(q(0,t),t) \\ q(y_\infty,t) &= q_\infty. \end{aligned}$$

The PDE under the change of coordinate is

$$\begin{aligned} \dot{q} &= e^{-z}\left(ae^{-z}q_z\right)_z + f \\ e^{-z}q_z(0,t) &= g_0(q(0,t),t) \\ q(y_\infty,t) &= q_\infty. \end{aligned}$$

Let $\Delta z$ be the grid spacing, and let $\delta = \Delta z/2$. For a node $k \in \{1,\ldots,K-1\}$, the PDE is semidiscretized as

$$\begin{aligned} \dot{q} = (\Delta z)^{-2} e^{-z_k}(&-a(z_k-\delta)e^{-(z_k-\delta)}(q_k - q_{k-1}) + \\ &a(z_k+\delta)e^{-(z_k+\delta)}(q_{k+1}-q_k)) + f(q_k,y_k). \end{aligned}$$

This discretization is a second-order-accurate conservative discretization of the gradient of the flux function $ae^{-z}q_z$. The boundary conditions are discretized as

$$e^{-z_0}\frac{q_1 - q_{-1}}{2\Delta z} = g_0(q_0), \qquad q_K = q_\infty.$$

The discretization of the Neumann boundary condition is a second-order-accurate approximation centered around $k = 0$.

We integrate the diffusion equations implicitly to avoid the Courant-Friedrichs-Lewy (CFL) time-step restriction on explicit methods, and we use the implicit-Euler method in particular. It is useful to view the resulting equations as a matrix equation. Let $\mathrm{bc}(\alpha,\beta) \equiv \begin{pmatrix}\alpha & 0 & \cdots & 0 & \beta\end{pmatrix}^T$. This vector is used to incorporate the boundary conditions. Let $A$ be the matrix that arises from the diffusion equation. Given a time interval $\Delta t$, let $\bar{A} \equiv I - \Delta t A$. Rearrangement of the discretized boundary conditions yields two scalars that must be incorporated into the matrix equation; we refer to these as

the Neumann factor nf and Dirichlet factor df. To take a step in time, the following system is solved:

$$\bar{A}q^{n+1} = q^n + f(q^{n+1}) + \Delta t \text{ bc}\left(\text{nf } g_0(q^{n+1}), \text{df } q_\infty\right).$$

**Implicit-explicit time integration.** Consider a semiexplicit index-1 differential algebraic equation (DAE) of the general form

$$\begin{aligned} 0 &= F(u,w,q,t) \\ \dot{w} &= G(u,w,q,t) \\ \dot{q} &= (aq_y)_y + f(u,w,q,t) \\ q_y(0,t) &= g_0(u,w,q(0,t),t) \\ q(y_\infty,t) &= q_\infty. \end{aligned} \tag{26}$$

$q$ is a diffusive quantity, $u$ is the vector of variables whose values are determined by algebraic equations, and $w$ is the vector of variables in first-order ODE. The zero- and finite-width models are each DAE in slip $\delta$, slip speed $v$, state $\theta$, porosity $\phi$, pressure $p$, and temperature $T$. Relative to (26), $w = \{\delta, \theta, \phi\}$, $q = \{p, T\}$, and $u = \{v\}$.

The time-stepping scheme must satisfy several objectives. First, $F = 0$ must be maintained to high precision. Second, $q$ must be integrated implicitly to avoid a stability-related time-step restriction. Third, it is preferable to integrate $w$ explicitly to avoid work associated with linear algebra. Fourth, the time step must be sensitive to $u$, $w$, and $q$.

Our method is built around a Runge-Kutta 2-3 pair (RK23) [34]. The second-order-accurate Runge-Kutta formula is used in the relative error control (REC) to determine the appropriate time step. Both the pair and the REC method are as implemented in MATLAB's `ode23`.

We take the time derivative of $F$ to obtain a first-order ODE in $u$. Two versions of $u$ are used: the DAE version, which always satisfies $F = 0$ to high precision; and the ODE version, which is used with $w$ in the REC and as an initial guess when solving $F = 0$.

RK23 has three stages in each time step. Consider a time step in which the time $t^n$ is advanced to time $t^{n+1}$. In this step, quantities are computed at the times $t^n < t_1^n < t_2^n < t^{n+1}$; and the stages advance from $t^n$ to $s$ for $s = t_1^n, t_2^n$, and $t^{n+1}$. $q^n$, $u^n$, and $w^n$ are known, and $u^n$ satisfies $F = 0$ to high precision. At each time *stage* $s$, $w(s)$ and the ODE version of $u(s)$ are available; and $\dot{u}(s)$, $\dot{w}(s)$, the DAE version of $u(s)$, and $q(s)$ must be computed. Using $w(s)$, $q^n$, and the ODE version of $u(s)$ as an initial guess, $F = 0$ and the implicit-Euler formula in $q$ are solved simultaneously for the DAE version of $u(s)$ and $q(s)$. Then $\dot{w}(s)$ and $\dot{u}(s)$ are computed using the DAE version of $u(s)$, $w(s)$, and $q(s)$. At the end of each time *step*, the ODE solver's version of $u$ is updated to be the DAE value.

**Factorization update.** Consider a general matrix $A$ for which we have a factorization $\text{fac}(A)$. Suppose column $i$ is altered to give the new matrix $\bar{A}$. A classical update to the factorization—called the *product-form* update in linear programming—follows. Let the new column $i$ be $v$, let $Au = v$, and let $T_i \equiv I + (u - e_i)e_i^T$, where $e_i$ is column $i$ of the identity matrix. Then $AT_i = A(I + (u - e_i)e_i^T) = \bar{A}$. The third term removes the old column $i$ from $A$, and the second term adds the new column.

To solve $\bar{A}x = b$, first solve $\text{fac}(A)u = v$, then solve $\text{fac}(A)T_i x = b$, where $T_i$ is a function of $u$. For $A \in \mathbb{R}^{n\times n}$, solving $T_i x = b$ requires a small factor of $n$ operations.

**Our model.** In this section we discretize the equations for the finite-width shear zone. The organization of the computations decouples the pressure, temperature, and momentum balance equations by cell. For a particular fault cell suppose we have $(p^{n-1}, T^{n-1})$ at time $t^{n-1}$, $(\delta^n, \theta^n, \phi^n)$ at time $t^n$, and we must determine $(v^n, p^n, T^n)$ at time $t^n$. Once these latter quantities are available, we can then provide the time derivatives of $\delta$, $\theta$, $\phi$, and $v$ (the latter for the purpose of REC) to the time-integration procedure. Here, $p_k$ is the perturbation from $p_\infty$. Let $\Delta t \equiv t^n - t^{n-1}$, $\sigma_b \equiv \sigma - p_\infty$, and $\bar{\sigma}^n \equiv \sigma_b - p_0^n$. We must solve the system of equations

$$\begin{aligned} \bar{A}_T T^n - T^{n-1} - \Delta t \text{ bc}\,(0, \text{df}_T\ T_\infty) - \Delta t \frac{\bar{\sigma}^n f(\theta^n, v^n) v^n}{h\rho c} g &= 0 \\ \bar{A}_p p^n - p^{n-1} - \Lambda(T^n - T^{n-1}) - \Delta t \text{ bc}\,(0, \text{df}_p\ p_\infty) + \frac{\dot{\phi}^n(\phi^n, v^n)}{\beta} g &= 0 \\ \tau^n - \bar{\sigma}^n f(\theta^n, v^n) - \eta v^n &= 0. \end{aligned}$$

The first two equations rearrange the implicit-Euler updates for $T$ and $p$. The final equation is the momentum balance equation.

In a typical simulation, several thousand nonlinear systems in several hundred variables must be solved at each stage. We solve each system using Newton's method. At each iteration of Newton's method, a linear system involving the Jacobian of the problem must be solved. The system is the following:

$$\begin{pmatrix} \bar{A}_T & \frac{\Delta t\ f^n v^n}{h\rho c} g e_1^T & -\frac{\Delta t\ \bar{\sigma}^n \left(\frac{\partial f^n}{\partial \psi^n} + f^n\right) v^n}{h\rho c} g \\ -\Lambda I & \bar{A}_p & \frac{\Delta t}{\beta} \frac{\partial \dot{\phi}^n}{\partial \psi^n} g \\ 0 & f^n e_1^T & -\bar{\sigma}^n \frac{\partial f^n}{\partial \psi^n} - \eta v^n \end{pmatrix} \begin{pmatrix} T^n + \Delta T^n \\ p^n + \Delta p^n \\ \Delta \psi \end{pmatrix} = \begin{pmatrix} T^{n-1} + \Delta t \text{ bc}\,(0, \text{df}_T\ T_\infty) + \frac{\Delta t\ \sigma_b f^n v^n}{h\rho c} g \\ p^{n-1} - \Lambda T^{n-1} + \Delta t \text{ bc}\,(0, \text{df}_p\ p_\infty) - \frac{\Delta t\ \dot{\phi}^n}{\beta} g \\ -\tau^n + \sigma_b f^n + \eta v^n \end{pmatrix},$$

where $\psi = \ln(v/v_0)$ and $f^n \equiv f(\theta^n, v^n)$. At fault cells away from the rupture tip, one to three Newton iterations are required; near the rupture tip, approximately five. It turns out that we can group fault cells by certain physical properties, perform only one sparse LU factorization per group, and update the factorization to solve each linear system. Two columns of the Jacobian must be modified. The factorization of the Jacobian is updated for each cell and then at each Newton iteration. For a fault having uniform properties, this

method's complexity scales linearly in both the number of fault cells and the number of diffusion-profile nodes.

## Appendix B: Analytical Results for the Zero-Width Fault

To obtain analytical approximations, Laplace transform equations (4) and (6), leading to two coupled ODE's in $y$. The solution to the heat equation, evaluated on $y=0$, is

$$\hat{T}(y=0,s) = \frac{1}{2\rho c\sqrt{c_{\rm th}}}\frac{1}{\sqrt{s}}\widehat{\tau v},$$

where $\hat{}$ indicates Laplace transform, with $s$ the transform variable. The solution to the pore pressure equation yields

$$\hat{p}(y=0,s) = \frac{\Lambda\hat{T}(y=0,s)}{(1+\sqrt{c_{\rm hyd}/c_{\rm th}})} - \frac{1}{2\beta}\sqrt{\frac{h^2}{c_{\rm hyd}}}\frac{1}{\sqrt{s}}\widehat{\dot{\phi}(s)},$$

where $p$ is the perturbation from the background pore-pressure. In the absence of dilatancy, the pore pressure and temperature on the fault are proportional [12]. However, the effect of dilatancy is not to offset $p$ by $-\delta\phi/\beta$ as suggested in Rice [12], in which case the second term would be $-\widehat{\dot{\phi}(s)}/\beta s$.

To proceed further, we follow [12] and examine behavior for constant $f$ and $v$. In this case the equation for $\hat{T}(y=0,s)$ is

$$\hat{T}(0,s) = \frac{fv}{2\rho c\sqrt{c_{\rm th}}}\frac{1}{\sqrt{s}}\left[\frac{\sigma-p^\infty}{s} - \hat{p}(0,s)\right].$$

Eliminating $\hat{T}(0,s)$ from the previous two equations yields

$$\hat{p}(0,s) = \frac{(\sigma-p^\infty)/s}{\sqrt{\frac{Ls}{v}}+1} - \frac{\omega\widehat{\dot{\phi}(s)}}{\sqrt{\frac{Ls}{v}}+1},$$

where $\omega = \frac{1}{2\beta}\sqrt{\frac{h^2 L}{c_{\rm hyd} v}}$ and

$$L = \left[\frac{2}{f}\frac{\rho c}{\Lambda}\frac{(\sqrt{c_{\rm th}}+\sqrt{c_{\rm hyd}})}{\sqrt{v}}\right]^2$$

is a characteristic length scale [12]. The non-dilatancy term for $p$ inverts as $p_{nd}(0,t) = (\sigma-p^\infty)[1-\exp(\delta/L)\mathrm{erfc}(\sqrt{\delta/L})]$, where $\delta = vt$ [12]. The dilatancy term can be approximated in the limit that $\phi$ evolves over a characteristic slip scale much shorter than $L$. We thus approximate, for $v/L \ll s$,

$$\begin{aligned}-\frac{\omega\widehat{\dot{\phi}(s)}\sqrt{v/L}}{\sqrt{s}(1+\sqrt{\frac{v}{Ls}})} &\approx -\omega\widehat{\dot{\phi}(s)}\frac{\sqrt{v/L}}{\sqrt{s}}\left[1-\sqrt{\frac{v}{Ls}}+\right.\\ &\qquad\left.\frac{v}{Ls}+O((v/Ls)^{3/2})\right]\\ &= -\omega\widehat{\dot{\phi}(s)}\sqrt{v/L}\left[\frac{1}{\sqrt{s}}-\sqrt{\frac{v}{L}}\frac{1}{s}+\frac{v}{Ls^{3/2}}+O((v/L)^{3/2}s^{-2})\right].\end{aligned}$$

Considering that $\phi$ evolves over distance scales $d_c$, we examine the following $\dot{\phi}(t) = \delta\phi_{\max}(v/d_c)(vt/d_c)\exp(-vt/d_c)$, such that $\widehat{\dot{\phi}(s)} = \delta\phi_{\max}(v/d_c)^2/(s+v/d_c)^2$. Inverting the leading two terms in the expansion yields an approximation to the dilatancy-induced pore pressure

$$\begin{aligned}p_d(0,t) \approx -\frac{\delta\phi_{\max}}{2\beta}\sqrt{\frac{h^2 v}{\pi c_{\rm hyd} d_c}}&\left[(1+2\delta')D(\sqrt{\delta'})-\sqrt{\delta'}\right.\\ &\left.+\sqrt{\frac{\pi d_c}{L}}\left(1-e^{-\delta'}-\delta' e^{-\delta'}\right)\right],\end{aligned}$$

where $\delta' = \delta/d_c$, and $D(z)$ is Dawson's integral: $D(z) = e^{-z^2}\int_0^z e^{t^2}dt$ . Comparisons to numerical inverse Laplace transforms shows that the approximation with the leading two terms accurately recovers the peak suction for $d_c/L = 0.01$, but underpredicts the peak suction by about 10% for $d_c/L = 0.1$.

The peak of the leading term in brackets is $\sim 0.85$ at $\delta/d_c \simeq 2.2$. For $h = 100\mu$m, $d_c = 20\mu$m, and $c_{\rm hyd} = 1\times 10^{-6}$m$^2$/s, $v = 1$m/s, $\sqrt{h^2 v/\pi c_{\rm hyd} d_c}/2 \simeq 6.3$, so that the induced pressure substantially exceeds $-\delta\phi_{\max}/\beta$. For $\phi_{\max} = 6\times 10^{-4}, \beta = 6\times 10^{-5}$ 1/MPa, then $-\delta\phi_{\max}/\beta \simeq 10$MPa, and thus can be of the order of $(\sigma - p^\infty)$.

To estimate the temperature, we use the second equation of this appendix to write

$$\hat{T}(0,s) = (1+\sqrt{c_{\rm hyd}/c_{\rm th}})\Lambda^{-1}\left[\hat{p}(0,s)+\frac{\omega\widehat{\dot{\phi}(s)}\sqrt{v/L}}{\sqrt{s}}\right].$$

Thus, the leading term in the dilatancy expansion cancels in the temperature and

$$\begin{aligned}\hat{T}(0,t) \approx \frac{(1+\sqrt{c_{\rm hyd}/c_{\rm th}})}{\Lambda}&\left\{(\sigma-p^\infty)[1-e^{\delta/L}\mathrm{erfc}(\sqrt{\delta/L})]\right.\\ &\left.+\frac{\delta\phi_{\max}}{2\beta}\sqrt{\frac{h^2 v}{c_{\rm hyd} L}}\left(1-e^{-\delta'}-\delta' e^{-\delta'}\right)\right\}.\end{aligned}$$

At the same order of expansion the temperature is less accurate than the pore pressure. Retaining the first three terms in the Taylor series, the maximum temperature is accurate to 3% when $d_c/L = 0.01$, but is off by $\sim 20\%$ when $d_c/L = 0.1$.